Ref. Ares(2026)5398993 - 28/05/2026

OPINCHARGE

Deliverable D5.1

SEI Modelling – Improved SEI Growth Models

05/2026

Funded by the European Union

Lead Beneficiary	German Aerospace Center (DLR)
Author(s)/Organisation(s)	Lukas Köbbing, Birger Horstmann (DLR), Ioannis Ypsilantis, William Gomes, Diego del Olmo, Beñat Larrarte-Lizarralde, Olatz Leonet, Elixabete Ayerbe (CIDETEC)
Contact Email	lukas.koebbing@dlr.de, birger.horstmann@dlr.de
Work Package	WP5
Delivery Date (DoA)	31/05/2026

NOTICE

Funded by the European Union under grant agreement number 101104032. Views and opinions expressed are however those of the author(s) only and do not necessarily reflect those of the European Union or European Climate, Infrastructure and Environment Executive Agency (CINEA). Neither the European Union nor the granting authority can be held responsible for them.

OPINCHARGE

Grant Agreement: 101104032.

Call: HORIZON-CL5-2022-D2-01.

Topic: HORIZON-CL5-2022-D2-01-02.

Type of action: HORIZON Research and Innovation Actions.

Granting authority: European Climate, Infrastructure and Environment Executive Agency.

Grant managed through EU Funding & Tenders Portal: Yes (eGrants).

Project starting date: fixed date: 1 June 2023.

Project end date: 31 May 2026.

Project duration: 36 months.

Copyright notice: © OPINCHARGE Consortium, 2023 - 2026.

Table of Contents

1 Introduction 5

2 Details on the performed work 5

2.1 SEI growth and degradation of Si-Gr composite anodes (DLR) 5

2.1.1 Model 5

2.1.2 Results 7

2.2 SEI growth simulations via kMC (CIDETEC) 9

2.2.1 Simulation results 10

2.3 Experimental validation (CIDETEC) 13

2.3.1 Feature Engineering 14

2.3.2 Data Acquisition and Generation 14

2.3.3 Machine Learning 14

2.3.4 Model Comparison 15

2.3.5 Results 15

2.4 Cell Testing (CIDETEC) 16

3 Summary 18

4 References 19

List of Figures

Figure 1 Illustration of (a) continuous SEI growth and crack opening, (b) crack propagation and island formation, (c) instantaneous SEI formation, and (d) details of crack propagation causing the instantaneous SEI formation 6

Figure 2 Capacity loss and loss of silicon during check-up cycling. (a) Capacity loss due to continuous and instantaneous SEI growth as well as loss of silicon. (b) Loss of silicon. 7

Figure 3 Capacity loss and loss of silicon during cycling between 40% and 80% SoC. (a) Capacity loss due to continuous and instantaneous SEI growth as well as loss of silicon. (b) Loss of silicon. 8

Figure 4 Simulated versus measured (a) capacity loss and (b) loss of silicon for cells with various cycling protocols and temperatures. 8

Figure 5 Left: hierarchical BKL scheme implemented in the kinetic Monte Carlo model. Right: flow diagram of the kMC algorithm 9

Figure 6 Evolution of the SEI thickness with time during the first lithiation of the anode (formation) at two different C-rates (top: C/10, bottom: C/3). The figures on the right show the time in logarithmic scale highlighting the onset of the main reactions (which correspond to the inflexion points on the SEI thickness evolution) 11

Figure 7 Top time evolution of the SEI composition obtained from the kMC model. Bottom: three representative snapshots extracted from the simulation at different formation times highlighting the figure highlights the distinction between the newly formed superficial SEI region and the consolidated inner SEI layer 12

Funded by the European Union

OPINCHARGE

Figure 8 Time evolution of the simulated SEI growth obtained from the kMC model during two full charge/discharge formation cycles at C/3 13
Figure 9 Schematic representation of the proposed automated EIS modelling pipeline.....14
Figure 10 Comparison of impedance analysis results obtained using the current framework (labelled as Impedix), RelaxIS and AutoEIS. The subplots show (a) Nyquist representation of the measured and fitted spectra and (b) the corresponding Bode phase plot. Despite differences in equivalent circuit formulations across the tools, the main electrochemical features of the impedance response are consistently captured 15
Figure 11 Estimation of the SEI-related resistance contribution from fitted EIS spectra. Representative fitted Nyquist spectra are shown for two cell configurations: SiPAA || Li (left) and Li || LMFP (right), both measured using 1 M LiPFP6 in EC:DMC 1:1 with 2 wt.% VC as electrolyte.....16
Figure 12 NanoSi-based anodes validated in full cell configuration. a) cycling performance and b) Coulombic efficiency of the FCC cycled at 0.5C with characterization cycle at 0.05C. 1C = 150 mAh g-1. REF = 1M LiPF6 in EC:DMC 1:1 (w/w). VC = Ref + 2 wt.% VC. FEC = Ref + 2 wt.% FEC.....17
Figure 13 Nyquist plots of a) Si(PAA), b) LMFP and c) LMFP || Si(PAA) FCC. d) Equivalent circuit used in the EIS fitting. 50%SoC. Electrolyte VC. Inset: Bode phase plot.....18

Funded by the European Union

1 Introduction

Deliverable Name:

"SEI Modelling – Improved SEI Growth Models"

The growth of the Solid-Electrolyte Interphase (SEI) is typically the most dominant degradation mechanism in state-of-the-art lithium-ion batteries. Understanding the processes causing SEI growth from a model perspective helps to find strategies to mitigate the ongoing degradation.

We have developed improved SEI growth models on different levels. The DLR has investigated the degradation of cells with silicon-graphite composite anodes by considering continuous SEI growth as well as instantaneous SEI growth and loss of silicon due to particle cracking in a continuum model. While CIDETEC complements this study with kinetic Monte-Carlo model for SEI growth simulations, automatic EIS methodology to extract SEI resistance, and cell testing of OPINCHARGE materials to validate or feed these models.

Our insights significantly improved the modelling and understanding of SEI growth. The details of the developed models are described in the following.

2 Details on the performed work

We have approached and achieved the deliverable from different perspectives. Here, we describe the details on the performed work of the contributing partners.

2.1 SEI growth and degradation of Si-Gr composite anodes (DLR)

Achieving higher energy density and extended lifetime are critical requirements for next-generation lithium-ion batteries. Silicon has emerged as a promising anode material due to its high specific capacity. However, its substantial volume expansion and contraction during lithiation and delithiation processes significantly compromise battery longevity. Thus, instead of pure silicon anodes, state-of-the-art lithium-ion batteries use silicon graphite composite anodes with a small silicon share. A comprehensive physical understanding of degradation mechanisms is therefore essential to advance the field. In this section, we present a physics-based model that describes battery degradation focusing on Silicon-graphite composite anodes under diverse cycling protocols, including the impact of regular check-ups. Our approach enables the separation and identification of fundamental degradation mechanisms, especially continuous and instantaneous Solid-Electrolyte Interphase (SEI) growth as well as loss of silicon. We systematically investigate how check-ups and operating conditions influence the observed degradation and elucidate the underlying causes of accelerated degradation in batteries incorporating silicon in their anodes. Our insights provide a foundation for future optimization of battery usage and design. A manuscript describing the model and the results is submitted and a pre-print is uploaded to ArXiv.[1]

2.1.1 Model

To describe the degradation behaviour of silicon-containing anodes, we consider several degradation pathways, which are illustrated in Figure 1. On the one hand, the contact of active material surface area with liquid electrolyte leads to continuous SEI growth. The SEI consumes lithium that is

Funded by the European Union

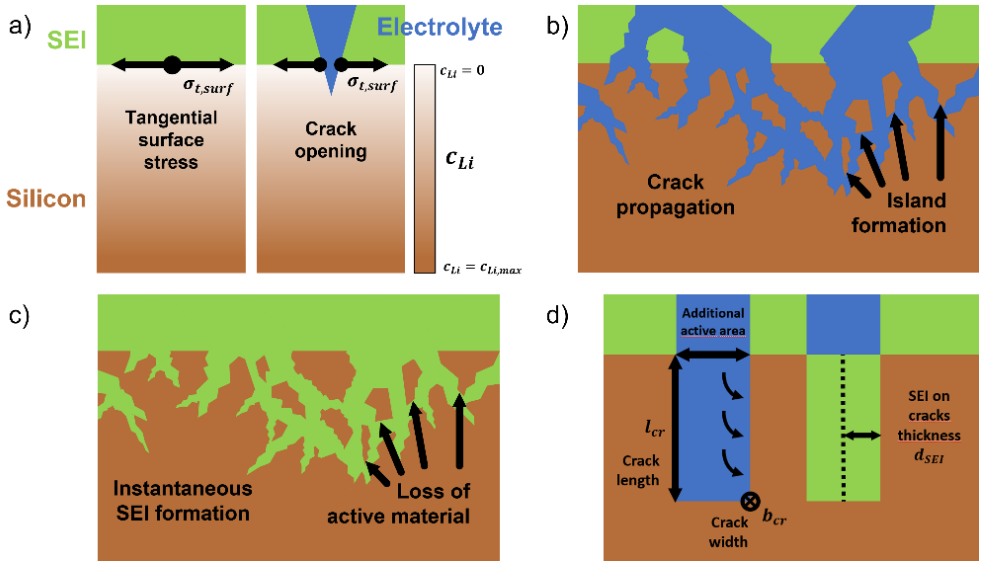

Figure 1 Illustration of (a) continuous SEI growth and crack opening, (b) crack propagation and island formation, (c) instantaneous SEI formation, and (d) details of crack propagation causing the instantaneous SEI formation

subsequently no longer available for battery operation. On the other hand, the silicon particles show tremendous volume changes accompanied by severe stresses during cycling, causing the generation of cracks inside these particles. These cracks expose fresh, unprotected crack surface to the electrolyte, leading to instantaneous SEI growth inside the cracks. Moreover, the accumulation of cracks throughout the silicon particles results in island formation of inactive silicon, losing the electrical contact. The details of the model are presented in the following.

The active surface area of the anode contributes to capacity fade via continuous SEI growth. This type of SEI growth is mediated by the diffusion of electrons through the SEI. The current density $j_{\mathrm{SEI,ED}}$ due to continuous SEI growth on the anode active surface area via electron diffusion is described by

$$j_{\mathrm{SEI,ED}} = \frac{c_{\mathrm{e^-}} D_{\mathrm{e^-}} F}{L_{\mathrm{SEI}}} \exp(-\tilde{\eta}_{\mathrm{SEI}})$$

with the reference concentration of electrons at the anode-electrolyte interface $c_{\mathrm{e^-}}$, the diffusion coefficient of electrons $D_{\mathrm{e^-}}$, the Faraday constant F, the thickness of the SEI L_{SEI}, and the SEI overpotential $\tilde{\eta}_{\mathrm{SEI}}$.

Regarding the stresses inside the silicon particles during cycling, our model considers the generation of cracks, which cause instantaneous SEI growth as well as loss of silicon as active anode material. The generation of cracks expressed by the crack length l_{cr} is described by

$$\partial_t l_{\mathrm{cr}} = k_{\mathrm{cr}} \sigma_{\mathrm{t}}^m$$

with the rate constant for the crack evolution k_{cr} and the tangential surface stress of the silicon particles σ_{t}, weighted by a fixed exponent m.

As the cracks expose fresh anode surface to the electrolyte, their generation causes instantaneous SEI growth. The current density $j_{\mathrm{SEI,crack}}$ due to instantaneous SEI growth on SEI cracks is described by

$$j_{\mathrm{SEI,crack}} = \frac{F}{V_{\mathrm{SEI}}} \frac{\partial_t l_{\mathrm{cr}}}{l_{\mathrm{cr}}} d_{\mathrm{SEI}}$$

with the mean molar volume of the SEI V_{SEI} and the instantaneous SEI thickness due to electron tunnelling d_{SEI}.

Funded by the European Union
OPINCHARGE

In addition, the cracks cause loss of active silicon, as the cracks can propagate through the whole silicon particles. The evolution of the active silicon content ϵ_{Si} due to crack formation is expressed by

$$\partial_t \epsilon_{\mathrm{Si}} = -k_{\mathrm{LAM}} \sigma_{\mathrm{t}}^{m} \epsilon_{\mathrm{Si}}$$

with the rate constant for the loss of silicon active material k_{LAM}.

Depending on the cycling conditions, these degradation effects – namely continuous SEI growth, instantaneous SEI growth, and loss of silicon active material – contribute in different amount to the total capacity loss observed in experiments. Understanding the cause for capacity loss under various cycling conditions can help to mitigate the most detrimental effects by cell engineering or adjustment of the cycling conditions to prolong battery lifetime.

2.1.2 Results

In this section, we investigate the simulated capacity loss by our model in comparison to the experimentally observed capacity loss under different cycling conditions. The experimental results are taken from literature.[2–4] In all these experiments, check-up cycles are performed regularly to be able to estimate the capacity loss.

The check-up cycles influence the degradation in all measurements. Thus, we investigate the degradation taking place during the check-up cycles in Figure 2. As demonstrated in Figure 2(a), the capacity loss during the check-ups is dominated by instantaneous SEI growth on silicon cracks. Additionally, Figure 2(b) shows that the cell loses around 30% of their silicon content after only 50 check-ups, which correspond to roughly 150 full cycles. The generation of cracks leading to instantaneous SEI growth and loss of silicon is strongly pronounced during the check-up cycles, as low SoC values are reached in every cycle, leading to increased surface tangential stress and fast crack propagation.

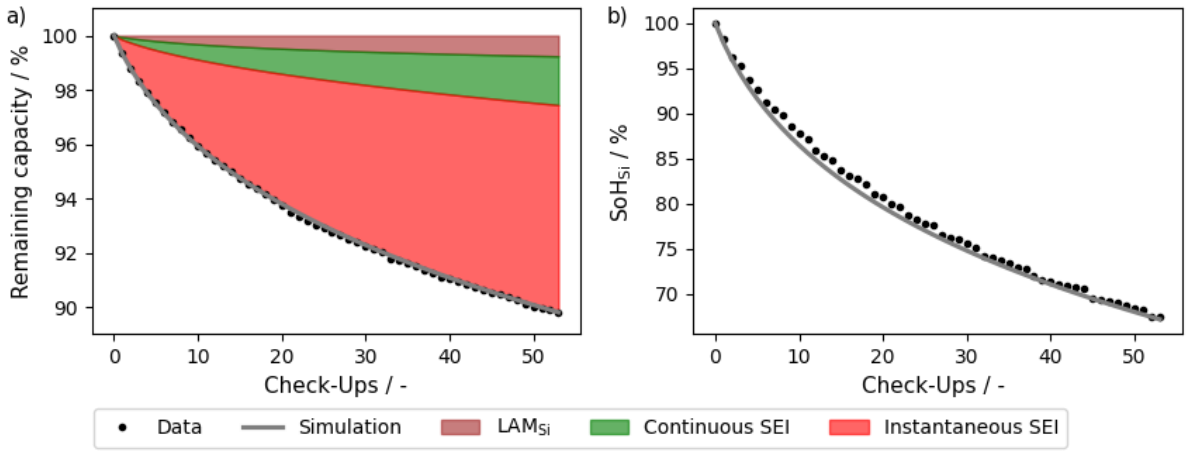

Figure 2 Capacity loss and loss of silicon during check-up cycling. (a) Capacity loss due to continuous and instantaneous SEI growth as well as loss of silicon. (b) Loss of silicon.

After discussing the degradation during the check-ups, we investigate the degradation during cycling in intermediate or slightly elevated SoC regions. We depict the simulated capacity loss for a cell cycling between 40% and 80% SoC in Figure 3. For this cycling condition, Figure 3(a) shows the contributions of the different degradation mechanisms to the total capacity loss. In contrast to the degradation during the check-up cycles, the degradation observed during regular cycling constitutes of similar amount of continuous and instantaneous SEI growth. Considering the dominance of instantaneous SEI growth during the check-up cycles contributing to the observed capacity loss, we can conclude that the degradation during cycling in the 40% to 80% SoC region (excluding the checkups) is clearly

Funded by the European Union
OPINCHARGE

dominated by continuous SEI growth. Figure 3(b) illustrates the loss of silicon simulated for the cycling protocol. Comparing the loss of silicon during the complete protocol (purple line) to the loss of silicon during the check-ups only, reveals only a minor difference. This confirms that the silicon particle cracking and the associated instantaneous SEI growth predominantly occurs during the check-ups and occurs only rarely during cycling in intermediate or slightly elevated SoC regions.

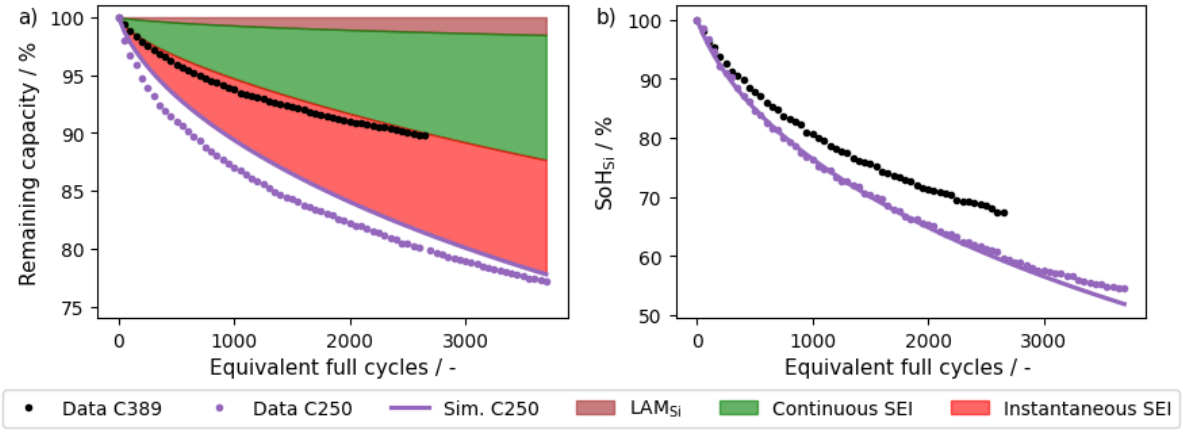

Figure 4 Capacity loss and loss of silicon during cycling between 40% and 80% SoC. (a) Capacity loss due to continuous and instantaneous SEI growth as well as loss of silicon. (b) Loss of silicon.

To further validate our model, we compare the simulated and the measured capacity loss and loss of silicon for various cells in Figure 4. This figure contains data for various cycling protocols, varying the charge and discharge rate, minimum and maximum SoC during cycling, as well as the temperature. Both measures, capacity loss and loss of silicon, show a good agreement between simulation and experiment, confirming the validity of our model results. Hence, we have presented a model that accurately describes capacity loss during cycling in form of continuous and instantaneous SEI growth as well as loss of active silicon anode material.

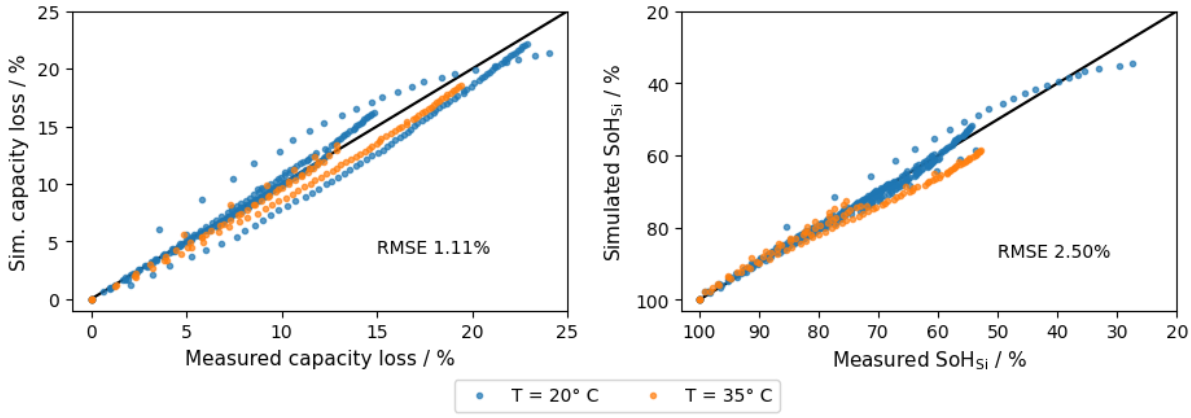

Figure 3 Simulated versus measured (a) capacity loss and (b) loss of silicon for cells with various cycling protocols and temperatures.

To conclude, we have presented a model describing the degradation of silicon-graphite composite anode driven by instantaneous and continuous SEI growth as well as silicon loss. Particularly, the share of instantaneous and continuous SEI growth on the total capacity loss is strongly dependent on the cycling conditions. Cycling in low SoC regions as performed during the check-ups causes pronounced stress and particle cracking, leading to a large amount of instantaneous SEI growth and loss of silicon. Contrarily, cycling in intermediate or slightly elevated SoC regions causes less particle cracking and increases the amount of continuous SEI growth. The achieved understanding of the different degradation pathways can help to find strategies mitigating these degradation mechanisms and

Funded by the European Union
OPINCHARGE

improving the cell's lifetime. A manuscript describing the model and the results is submitted and a pre-print is uploaded to ArXiv.[1]

2.2 SEI growth simulations via kMC (CIDETEC)

To investigate the growth of the solid electrolyte interphase (SEI) on the negative electrode at the mesoscopic scale, a kinetic Monte Carlo (kMC) model was developed. The kMC method is a stochastic, event-driven approach that can simulate the temporal evolution of chemical reactions based on their reaction rates, which are converted into event frequencies. Owing to the stochastic nature of the simulations, the reported results are typically obtained by averaging multiple simulation runs performed with different random seeds in order to estimate the overall system behaviour. The implementation developed within this project was based on several literature references[5,6,7].

The kMC implementation is based on a hierarchical Bortz–Kalos–Lebowitz (BKL) algorithm that combines process and spatial binning, ensuring that rate updates are performed locally. This strategy reduces the number of iterations required for event selection and system updates, thereby improving computational efficiency. The model accounts for reaction events, surface diffusion, and adsorption/clustering processes. In the implemented approach, only the electrode, SEI products, and reaction intermediates are explicitly represented as species occupying sites on the simulation grid. In contrast, the distributions of electrolyte and salt species are treated implicitly and estimated through probabilistic functions that depend on the instantaneous state of the simulation. The overall kMC workflow is summarized in Figure 5.

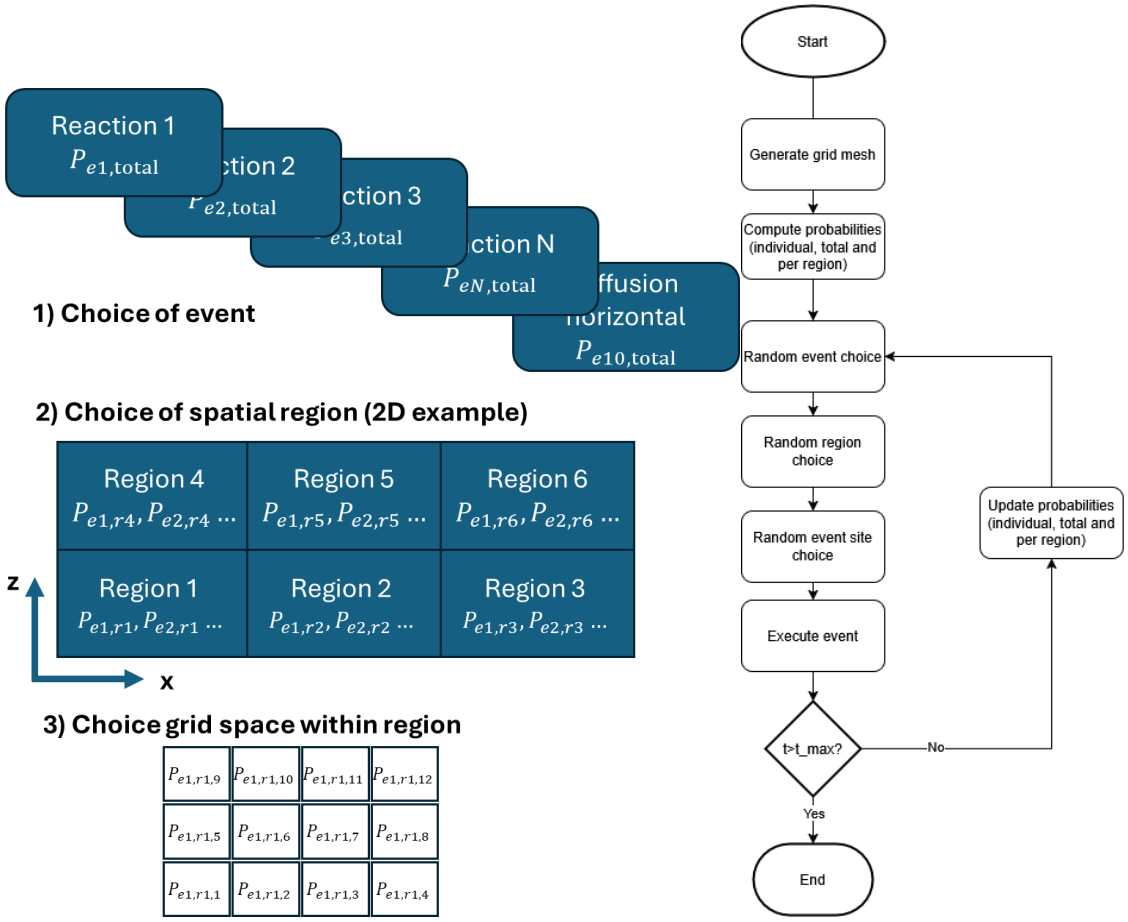

Figure 5 Left: hierarchical BKL scheme implemented in the kinetic Monte Carlo model. Right: flow diagram of the kMC algorithm.

Funded by the European Union
OPINCHARGE

The initial implementation of the model was developed in Python; however, its usability was limited by the relatively slow execution speed associated with the sequential nature of the kMC algorithm. To overcome this limitation, the core kMC routines were rewritten in C++, while maintaining a Python interface for user interaction and model configuration. This optimization increased the computational performance by approximately two orders of magnitude, reaching execution speeds of up to 104 kMC steps per second on a laptop equipped with an 11th Gen Intel® Core™ i7-1165G7 processor.

The final version enables the user to define the relevant reaction mechanisms and SEI species of interest and supports both two-dimensional and three-dimensional simulation grids through the Python interface. The rate of the reaction of the kMC events are defined by their reaction kinetics:

$$R_f = k_0 \, e^{-\frac{E_a}{RT}},$$

$$R_b = k_0 \, e^{-\frac{E_a}{RT}} e^{-\frac{\Delta_a G}{RT}}.$$

For the electrochemical reactions, the activation energy of the reaction will also depend on the potential of the electrode $\Delta\Phi$ such that $E_a = E_{a,0} + \alpha\Delta\Phi F$. Moreover, an extra term is added to electrochemical reactions to capture the effect of electron transport through the SEI which is proportional to the distance from the site to the anode surface (δ_p) so that:

$$\hat{R}_{f/b} = R_{f/b} \, e^{-\frac{\delta_p E_{a,\mathrm{SEI}}}{RT}}.$$

The reaction parameters, including kinetic constants and activation energies, are obtained from *ab initio* calculations and currently based on values collected from different literature sources. Moreover, although the temperature dependence is incorporated through the Arrhenius-type formulation, the temperature effects have not yet been fully validated. Note that, the framework is flexible to accommodate any set of reactions making it able to simulate any combination of negative electrode/electrolyte given that the reactions and their parameters are known.

Finally, the kMC model was coupled with a single-particle model (SPM) implemented in PyBaMM in order to track the evolution of the electrode potential during the formation cycle. The SPM is a simplified electrochemical model in which the electrodes are lumped as a single representative active material particle, assuming the main operational limitations arise from solid diffusion in the particle and interfacial kinetics. The coupling between the models enables a dynamic interaction between macroscale electrochemical behaviour and mesoscale SEI growth processes. The implemented coupling strategy, based on [7], consists in using the kMC model to provide the SPM with the evolving SEI thickness and composition, which influence the interfacial voltage drop. In turn, the SPM feeds back the negative electrode potential to the kMC model, thereby affecting the rates of electrochemical reduction reactions.

2.2.1 Simulation results

Figure 6 shows the evolution of the SEI thickness with time together with the voltage profile of the negative electrode during a formation charge. Following the model, the SEI grows rapidly initially when the potential of the electrode falls below the onset potential of the main reactions, this is in line with observed experimental measurements[8]. After this quick initial growth, there is a stabilization phase

Funded by the European Union

driven by the resistivity of the SEI which limits the ability of the electrons to reach the surface and lead to the solvent reduction.

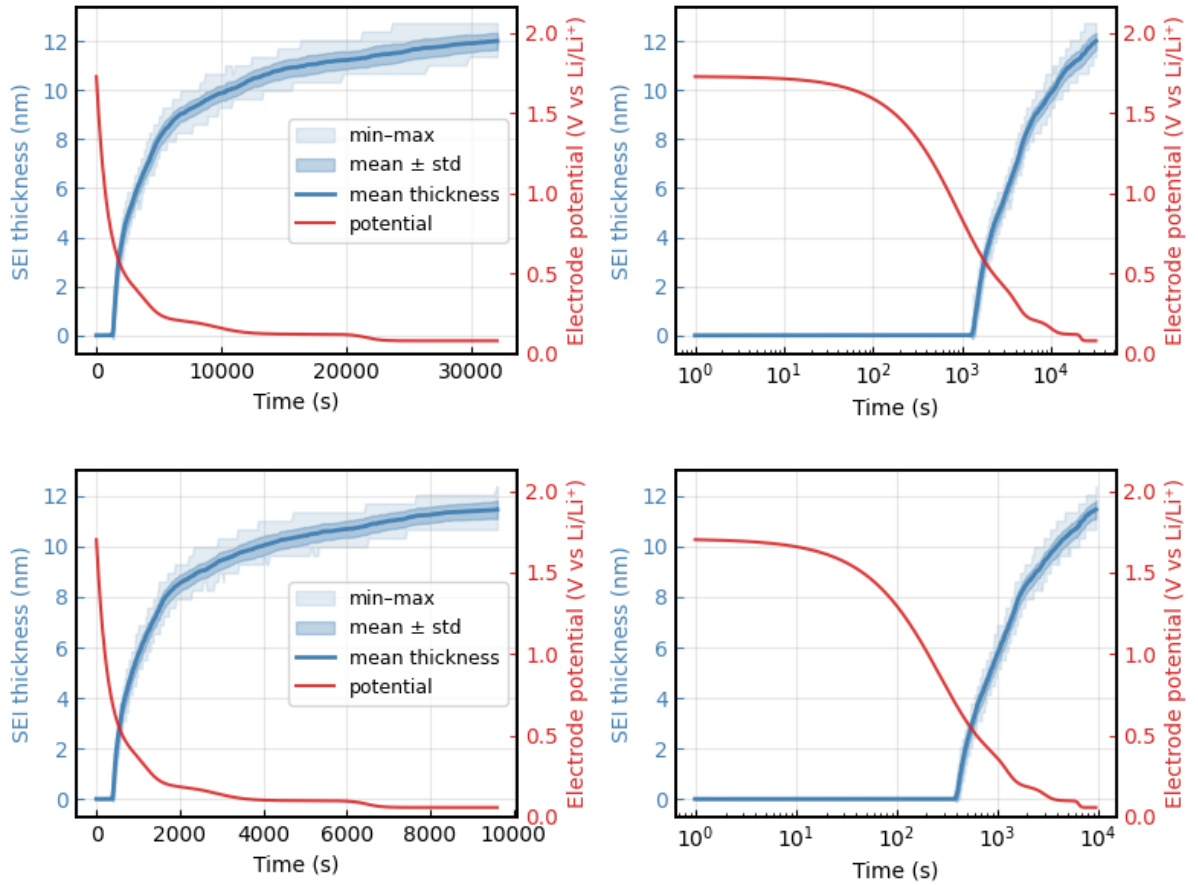

Figure 6 Evolution of the SEI thickness with time during the first lithiation of the anode (formation) at two different C-rates (top: C/10, bottom: C/3). The figures on the right show the time in logarithmic scale highlighting the onset of the main reactions (which correspond to the inflexion points on the SEI thickness evolution).

Figure 7 presents three representative snapshots extracted from the SEI growth simulation at different stages of the formation process. The results show that SEI growth occurs rapidly during the initial stages of formation, whereas the growth rate progressively decreases as the layer becomes thicker. In particular, the formation of the final nanometres of the SEI requires significantly longer simulation times, indicating that the growing SEI progressively limits further reaction and transport processes at the electrode interface. Additionally, the simulated SEI structure can be divided into two main regions: a superficial and dynamically evolving outer layer, and an inner consolidated SEI layer closer to the electrode surface. Newly formed SEI species initially accumulate in the superficial region and progressively transform into a denser and more consolidated structure as the simulation evolves.

Funded by the European Union

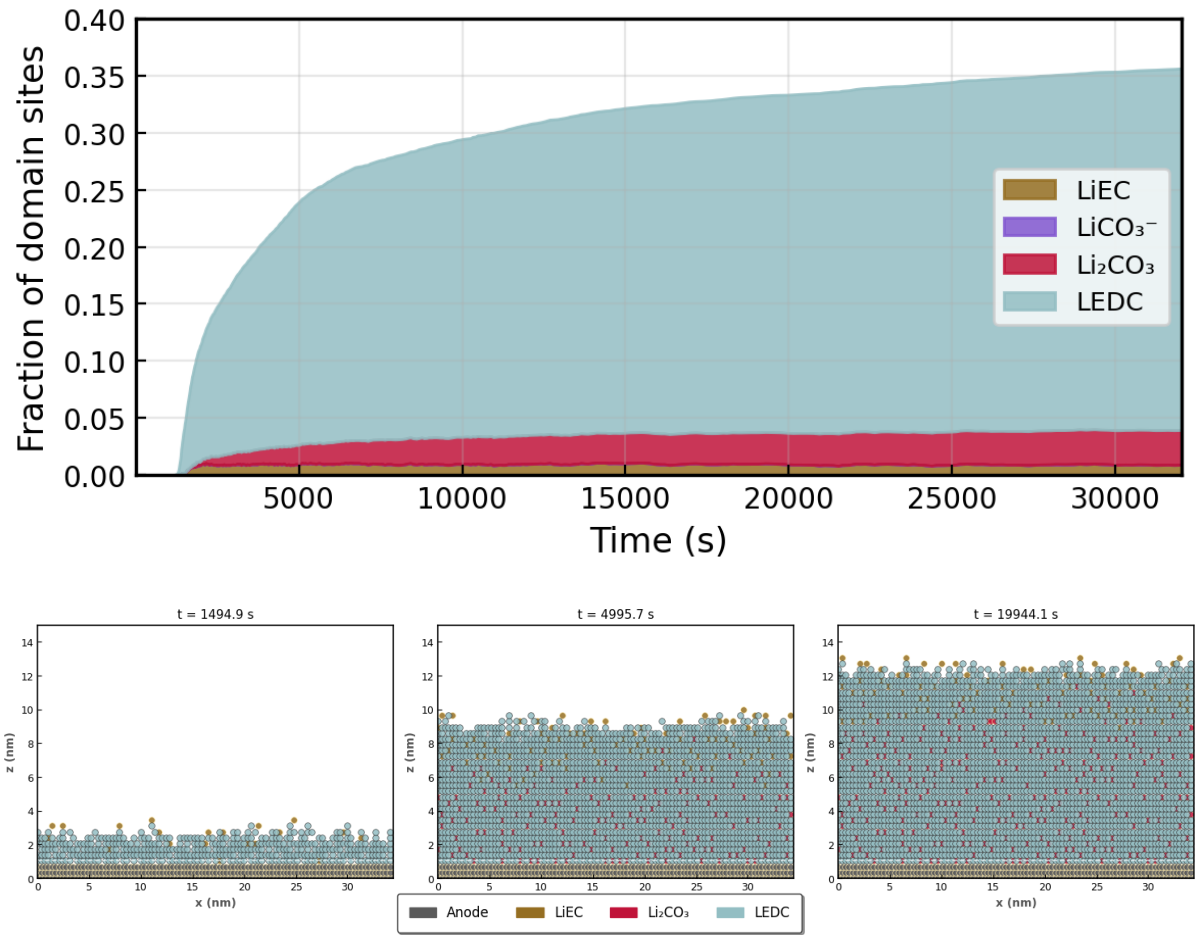

Figure 7 Top time evolution of the SEI composition obtained from the kMC model. Bottom: three representative snapshots extracted from the simulation at different formation times highlighting the figure highlights the distinction between the newly formed superficial SEI region and the consolidated inner SEI layer.

The model also enables the simulation of longer cycling protocols, for example, in Figure 8.a a full forming protocol consisting of two charge/discharge cycles is presented. It can be noted that in this case some of the SEI seems to be consumed at higher voltages (when the anode is almost depleted from lithium) which is related to the intermediates (such as LiEC) that can be reverted. The final solid SEI-forming species are assumed to be irreversible in this model. This trend is presented more clearly in Figure 8.b, where only the occupancy of intermediate species are the ones to drop.

Funded by the European Union
OPINCHARGE

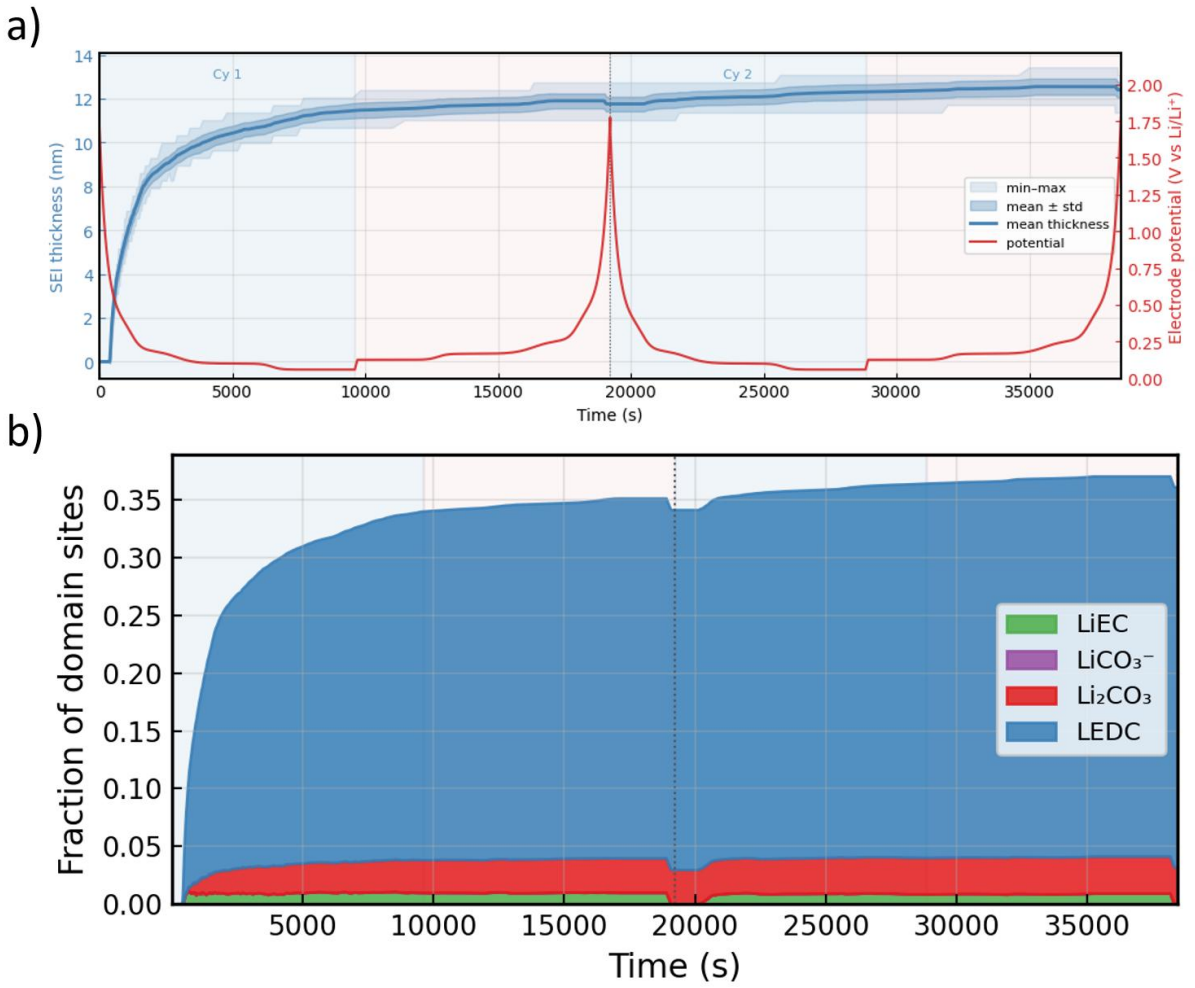

Figure 8 Time evolution of the simulated SEI growth obtained from the kMC model during two full charge/discharge formation cycles at C/3.

2.3 Experimental validation (CIDETEC)

The main goal of this study is to gain more understanding of the underlying mechanisms measured in EIS experiments. To do this, a new methodology was developed to automatically analyse EIS experiments by using Machine Learning models (MLMs) and Distribution of Relaxation Times (DRT), the deconvolution of impedance spectra. On one side, MLMs provide a probability-ranked shortlist of candidate Equivalent Circuit Models and initial estimates of the corresponding circuit parameters, whereas DRT is used to extract additional physics-informed descriptors from the raw impedance data. Figure 9 illustrates the overall modelling methodology.

Funded by the European Union

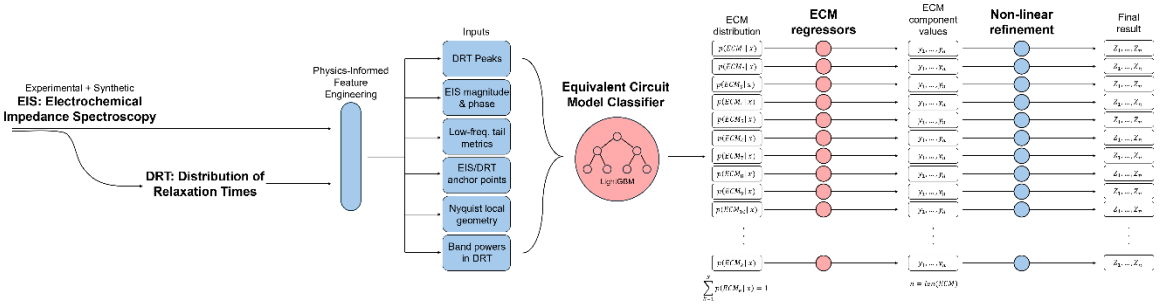

Figure 9 Schematic representation of the proposed automated EIS modelling pipeline

First, heterogeneous experimental and synthetic impedance spectra are unified, transformed via DRT, and mapped to physics-informed EIS/DRT features. Then, a LightGBM classifier estimates probabilities over candidate equivalent circuit topologies, while an auxiliary LightGBM process-count classifier refines the ranking through process-count-informed reranking. Topology-specific regressors provide initial parameter estimates, which are subsequently refined through complex non-linear least-squares fitting. Blue represents physics-based modelling, while red represents data-driven modelling.

2.3.1 Feature Engineering

On top of the canonical EIS and DRT representations, the tool computes a large collection of *physics-informed features* which serve as inputs to the machine-learning models, such as DRT peak information, EIS magnitude or low frequency tail metrics.

For machine-learning use, these physics-informed feature families were assembled into three fixed-width input representations. This organization allowed us to compare whether classifier and regressor performance benefited more from compact whole-spectrum encoding or from an explicit separation of arc- and tail-dominated behaviour.

2.3.2 Data Acquisition and Generation

A physics-guided, stochastic, synthetic data generator was used to simulate paired EIS and DRT responses from a registry of candidate ECM topologies. The synthetic dataset is used for model development, training, and held-out testing of the classifier and regression models, while the experimental dataset is employed for validation, ensuring an unbiased evaluation of model generalization under real measurement conditions.

The ECM generator is based on a registry of ECM topologies comprising combinations of series ohmic resistance R_0, multiple parallel $R-CPE$ or $R-C$ branches representing charge-transfer and interfacial processes, and diffusion-related elements such as semi-infinite Warburg components (W), finite-length Warburg elements (W_o and W_s), and Gerischer-type blocks (G and G_s). Parameter sampling follows structured design-of-experiments strategies, spanning several decades for resistances, pseudo-capacitances, CPE exponents, and diffusion coefficients using log-uniform and beta-distributed draws. Physical plausibility is enforced through global constraints on impedance characteristics, including bounds on total real resistance and maximum imaginary amplitude, ensuring that simulated spectra remain within realistic Nyquist envelopes.

2.3.3 Machine Learning

The LightGBM classifier with process-count-informed reranking showed a clear ability to capture meaningful relationships between impedance spectra and ECM topology. For the evaluation, 12% of

Funded by the European Union
OPINCHARGE

the synthetic dataset was used for testing and the remaining 88% for training. Across 29 ECM classes, the classifier achieved an exact top one accuracy of 68.7%, while the correct ECM was included among the top three recommendations in 92.8% of cases.

For each ECM topology in the registry, a dedicated LightGBM-based multi-output regressor is trained using only synthetic samples belonging to that topology. The regressors map the same feature vectors to parameter estimates $\widehat{\boldsymbol{\theta}}_{\boldsymbol{ML}}$. which are subsequently refined through CNLS fitting. For the calculation of the regression error metrics, 88% of the synthetic dataset was used for training and the remaining 12% for testing. The overall metrics were computed by first evaluating each ECM-specific regressor on its corresponding held-out synthetic samples and then taking the mean across the 29 ECM topologies. The resulting mean error metrics across all models were an R^2 score of 0.952, an RMSE of 0.643, and an MAE of 0.110.

2.3.4 Model Comparison

Figure 10 shows the comparison of the proposed modelling framework with RelaxIS, and AutoEIS using SiCMC||Li (1M LiPF6 in EC:DMC 1:1) CR2025 cell configuration assembled in Task5.4 by CIDETEC. The evaluation considers both the quality of the impedance reconstruction and the consistency of the extracted ECM parameters.

While the circuit topologies differ slightly across methods, all approaches reproduce the overall impedance response with high consistency. The current framework identifies the circuit $\boldsymbol{R0} - \boldsymbol{p}(\boldsymbol{R1}, \boldsymbol{CPE1}) - \boldsymbol{p}(\boldsymbol{R2}, \boldsymbol{CPE2}) - \boldsymbol{Gs0}$, whereas RelaxIS uses $\boldsymbol{R0} - \boldsymbol{p}(\boldsymbol{R1}, \boldsymbol{CPE1}) - \boldsymbol{p}(\boldsymbol{R2} - \boldsymbol{W1}, \boldsymbol{CPE2})$, and AutoEIS represents the system as $[\boldsymbol{P1}, \boldsymbol{P2}] - [\boldsymbol{P3}, \boldsymbol{R4}] - \boldsymbol{R5}$ according to its symbolic circuit notation. This difference on AutoEIS ECM is because it uses a fully automated, data-driven approach that generates circuit elements based on pattern recognition rather than conventional topologies.

Despite these differences, the reconstructed impedance spectra remain in close agreement, indicating that the dominant electrochemical processes are consistently captured across all models. Notably, the current framework replaces the Warburg diffusion element used in RelaxIS with a Gerischer-type diffusion element (Gs), providing an alternative yet physically meaningful description of diffusion-limited processes at low frequencies.

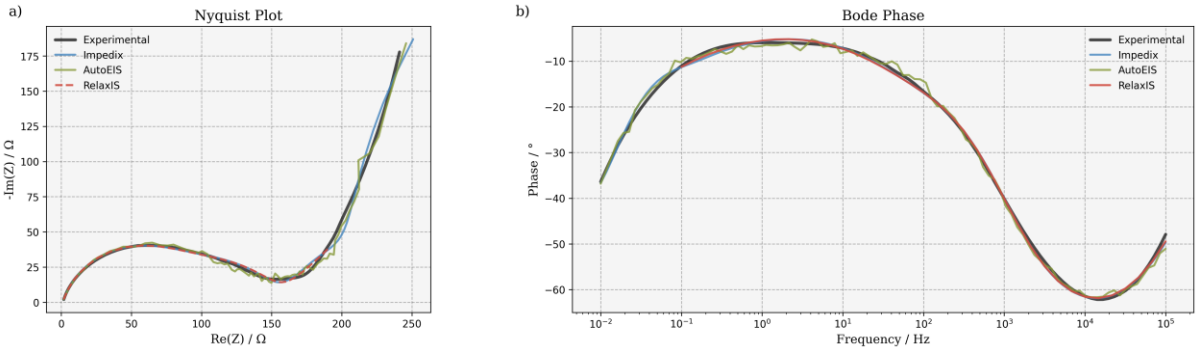

Figure 10 Comparison of impedance analysis results obtained using the current framework (labelled as Impedix), RelaxIS and AutoEIS. The subplots show (a) Nyquist representation of the measured and fitted spectra and (b) the corresponding Bode phase plot. Despite differences in equivalent circuit formulations across the tools, the main electrochemical features of the impedance response are consistently captured.

2.3.5 Results

After fitting the most suitable candidate ECMs, physically interpretable contributions are extracted. In particular, the high-frequency contribution is isolated from the Nyquist representation and reported as an estimated SEI resistance, R_{SEI}, providing a diagnostic quantity that can be compared across cells,

Funded by the European Union
OPINCHARGE

ageing states, and cycling conditions. This enables the study and monitoring of SEI-related resistance contributions.

Figure 11 shows the fitting results obtained using the tool on two example EIS experiments performed as part of Task 5.4. The highlighted SEI resistance span is obtained directly from the fitted high-frequency arc, while the remaining fitted response accounts for other interfacial and transport-related contributions. In this way, the framework provides both the full impedance reconstruction, and a specific SEI-related resistance estimate from the same fitted model.

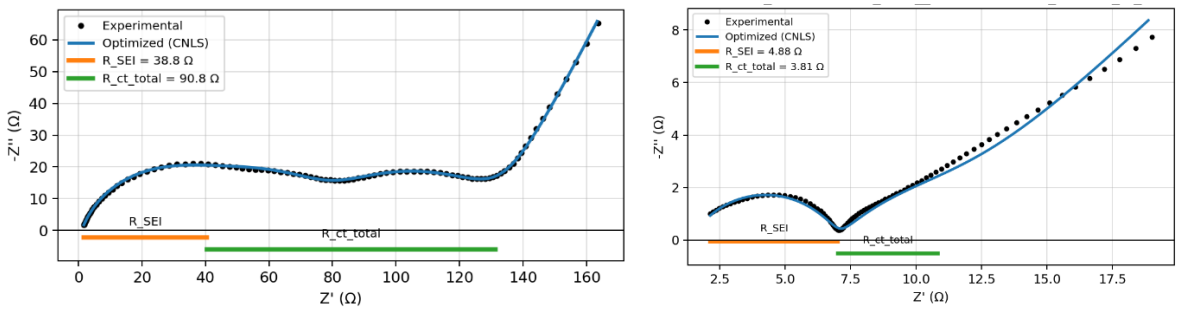

Figure 11. Estimation of the SEI-related resistance contribution from fitted EIS spectra. Representative fitted Nyquist spectra are shown for two cell configurations: SiPAA || Li (left) and Li || LMFP (right), both measured using 1 M LiPFP6 in EC:DMC 1:1 with 2 wt.% VC as electrolyte.

2.4 Cell Testing (CIDETEC)

In order to validate the models and electrodes developed in the project, half coin cells (HCC) were assembled using nanosilicon (Si(PAA)) and LMFP as positive electrodes, with thicknesses of 25 µm and 90 µm, respectively. The electrodes were punched to a diameter of 16.6 mm and vacuum-dried at 120 °C for 16 hours. Lithium (Albemarle®) disks, 18 mm in diameter and 50 µm thick, were used as the negative electrode. For the full coin cell (FCC) configuration, the LMFP electrode was punched to a diameter of 17.7 mm.

Cell assembly was carried out in a dry room with a dew point of −60 °C, using Whatman (GF/A) as the separator. Three electrolyte formulations were employed: 1 M $LiPF_6$ in EC:DMC (Solvionic), 1 M $LiPF_6$ in EC:DMC with 2% VC (Solvionic) and 1 M $LiPF_6$ in EC:DMC with 2% FEC (Solvionic). Galvanostatic and electrochemical impedance spectroscopy (EIS) measurements were subsequently performed at 25 °C using a Potentiostat/Galvanostat ZRA Interface 5000E (Gamry Instruments).

A current rate of C/40 was applied for silicon HCC and FCC cells, while C/20 was used for LMFP HCC to achieve the desired state of charge (SoC), also silicon and LMFP HCCs were cycle in the potential window of 0.005 – 1.20 V (vs Li^+/Li) and 2.80 – 4.20 V (vs Li^+/Li), respectively, while FCC cells were cycled in a window of 2.80 – 4.20 V. Impedance measurements were conducted by applying a 10 mV sinusoidal perturbation over a frequency range from 100 kHz to 100 mHz, with six points per decade. Prior to each measurement, the cells were allowed to rest for 2 hours to ensure steady-state conditions. Figures 12.a and 12.b shows the cycling performance and the coulombic efficiency of the FCC with three different electrolytes. It is observed that both additives helped to improve the capacities, with the VC electrolyte showing slightly better result. Abnormal behaviour is observed in the Coulombic efficiency of the cells containing REF electrolyte, possibly due to higher irreversible reactions at higher C-rate.

Funded by the European Union
OPINCHARGE

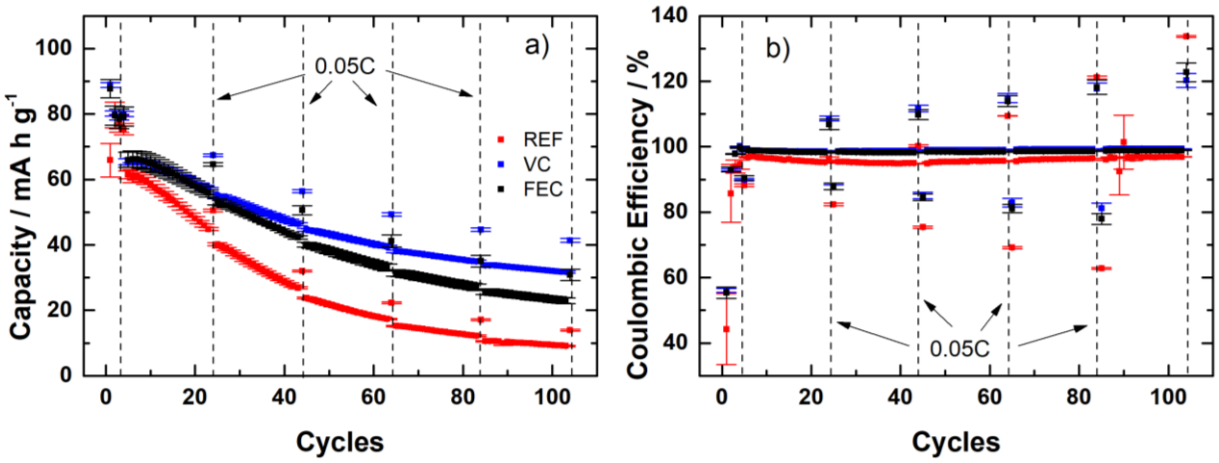

Figure 12 NanoSi-based anodes validated in full cell configuration. a) cycling performance and b) Coulombic efficiency of the FCC cycled at 0.5C with characterization cycle at 0.05C. 1C = 150 mAh g-1. REF = 1M LiPF6 in EC:DMC 1:1 (w/w). VC = Ref + 2 wt.% VC. FEC = Ref + 2 wt.% FEC.

Given the results obtained in the cycling tests, EIS analysis performed using VC electrolyte was chosen to be discussed further. The cells were cycled until the desired SoC, following the EIS measurement was performed after a proper resting period to avoid transient current which affects linearity and steady-state assumptions. Figure 13(a-c) shows the EIS profile of the nanoSi(PAA) and LMFP HCC, and LMFP|| Si(PAA) FCC at 50%SoC, respectively. The results were fitted with the equivalent circuit shown in Figure 13.d.

For the silicon HCC, figure 13.a, it is possible to identify two well-defined semicircles at high (10^5 – 10^3 Hz) and intermediate frequencies (10^1 – 10^0 Hz) associated with SEI and charge transfer reaction. The high values observed for these semicircles indicate sluggish kinetics for both processes, especially at the interface. At low frequencies (10^{-1} Hz) a straight line related to the diffusion impedance can be observed. As for the LMFP HCC, similar profile is observed with two semicircles at high and intermediate frequences associated to interface CEI and charge transfer reaction, respectively. Different from the silicon anode, the values of impedances of the LMFP HCC are almost ten times smaller, indicating that better kinetics for both interface and charge transfer processes. Lastly, a straight line related to diffusion impedance observed at low frequencies. In the of the LMFP the diffusion pattern approaches standard Warburg response of semi-infinite diffusion, while for the silicon HCC the diffusion pattern is closer to finite diffusion.

Finally, the FCC Nyquist plot presents two well-defined semicircles at high and intermediate frequencies, associated with the SEI and charge-transfer reactions, which can be confirmed by the Bode phase plot. The impedance values are significantly lower than those of the silicon HCC, which could indicate an interference from the Li metal electrode in the impedance response of the HCC. Nevertheless, the semicircle at intermediate frequencies is more predominant in the FCC, indicating that charge-transfer kinetics dominate the cell performance under this condition. Additionally, the low-frequency diffusion tail exhibits a behavior closer to finite diffusion. When comparing the HCC and FCC responses, it can be inferred that the nano Si(PAA) electrode dominates the overall impedance response of the FCC cell, particularly regarding the interfacial processes.

Funded by the European Union
OPINCHARGE

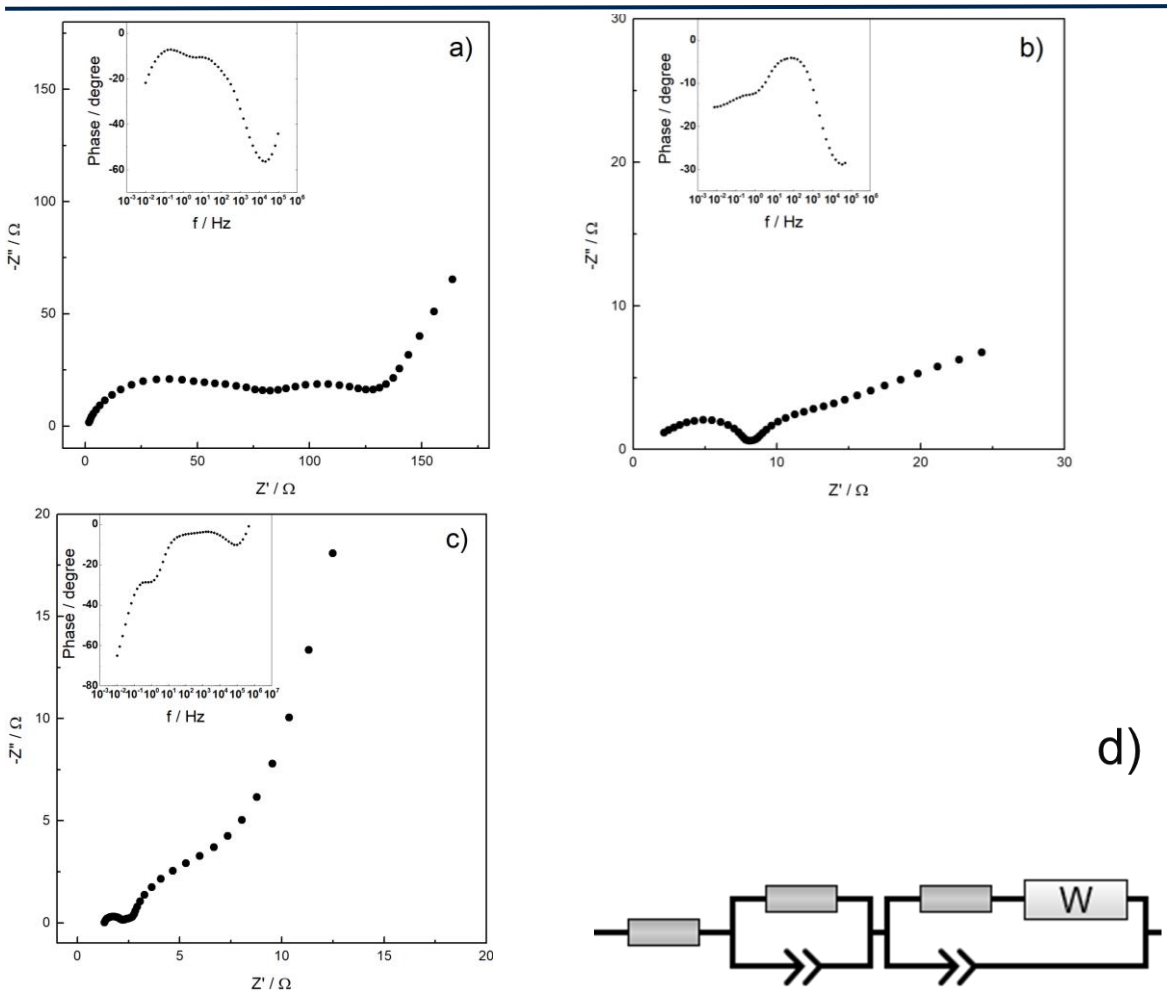

Figure 13 Nyquist plots of a) Si(PAA), b) LMFP and c) LMFP || Si(PAA) FCC. d) Equivalent circuit used in the EIS fitting. 50%SoC. Electrolyte VC. Inset: Bode phase plot.

3 Summary

As presented in this deliverable, we have developed new and improved SEI growth models focusing on different aspects that are relevant at different scales.

First, the DLR has developed an improved continuum model, accounting for continuous SEI growth as well as instantaneous SEI growth and loss of active material due to particle cracking. The simulations demonstrate that the instantaneous SEI growth on cracks is the dominating degradation mechanisms during check-up cycles covering the full SOC range. For cycling protocols in the intermediate SOC region, however, the continuous SEI growth is the prevailing mechanism. Therefore, the developed model demonstrates the relevance of the exact cycling protocol for the battery degradation.

Second, a kinetic Monte Carlo (kMC) model was developed to simulate SEI growth on the negative electrode, including reaction, diffusion, and adsorption processes. The implementation combines a C++ computational core with a Python interface, enabling efficient 2D and 3D simulations with flexible reaction mechanisms. The model was coupled with a PyBaMM single-particle model (SPM) to dynamically link SEI growth with electrode potential evolution during formation and cycling. Simulations reproduce the rapid initial SEI growth followed by stabilization due to transport

Funded by the European Union
OPINCHARGE

limitations, while also capturing SEI structural evolution and the reversible behaviour of intermediate species.

Third, an automated EIS analysis framework was developed combining machine learning models (MLMs) and Distribution of Relaxation Times (DRT) to identify equivalent circuit models (ECMs) and estimate their parameters. The methodology integrates physics-informed EIS/DRT features with LightGBM classifiers and regressors trained on a large synthetic dataset generated from physically realistic ECM topologies. The framework achieved high predictive performance, with the correct ECM identified within the top three recommendations in 92.8% of cases and accurate parameter estimation across 29 circuit classes. Comparison with RelaxIS and AutoEIS showed consistent impedance reconstruction despite differences in circuit formulations. The fitted models also enable extraction of physically interpretable quantities, such as the SEI-related resistance contribution, providing a diagnostic metric for analysing ageing and cycling effects.

Four, the electrodes were validated in both half-cell and full-cell configurations using CCCV cycling protocols. In addition, EIS measurements were performed at different states of charge. The impedance results revealed that the silicon electrodes dominate the cell kinetics, particularly the interfacial processes. The obtained results were subsequently used to validate the models developed within the framework of the project.

In summary, the developed improved SEI growth models have established a better understanding of the processes driving SEI growth and the degradation of lithium-ion batteries. This understanding will help to find strategies to mitigate the degradation pathways and improve the lifetime of silicon-containing cells.

4 References

(1) Philipp, M. C. J.; Köbbing, L.; Karger, A.; Jossen, A.; Latz, A.; Horstmann, B. Physics-Based Modeling of Cyclic and Calendar Aging of LIBs with Si-Gr Composite Anodes. *arXiv* **2026**.

(2) Karger, A.; Schmitt, J.; Kirst, C.; Singer, J. P.; Wildfeuer, L.; Jossen, A. Mechanistic Cycle Aging Model for the Open-Circuit Voltage Curve of Lithium-Ion Batteries. *J. Power Sources* **2024**, *593* (December 2023), 233947. https://doi.org/10.1016/j.jpowsour.2023.233947.

(3) Karger, A.; Schmitt, J.; Kirst, C.; Singer, J. P.; Wildfeuer, L.; Jossen, A. Mechanistic Calendar Aging Model for Lithium-Ion Batteries. *J. Power Sources* **2023**, *578* (May), 233208. https://doi.org/10.1016/j.jpowsour.2023.233208.

(4) Wildfeuer, L.; Karger, A.; Aygül, D.; Wassiliadis, N.; Jossen, A.; Lienkamp, M. Experimental Degradation Study of a Commercial Lithium-Ion Battery. *J. Power Sources* **2023**, *560* (January), 232498. https://doi.org/10.1016/j.jpowsour.2022.232498.

(5) Gerasimov, M.; Soto, F. A.; Wagner, J.; Baakes, F.; Guo, N.; Ospina-Acevedo, F.; Röder, F.; Balbuena, P. B.; Krewer, U. Species distribution during solid electrolyte interphase formation on lithium using MD/DFT-parameterized kinetic Monte Carlo simulations. The Journal of Physical Chemistry C, 2023, vol. 127, no 10, p. 4872-4886.

(6) Esmaeilpour, M.; Jana, S.; Li. H.; Solymanibrojeni, M.; Wenzel, W. A Solution-Mediated Pathway for the Growth of the Solid Electrolyte Interphase in Lithium-Ion Batteries. Advanced Energy Materials, 2023, vol. 13, no 14, p. 2203966.

(7) Röder, F.; Braatz, R. D.; Krewer, U.. Multi-scale simulation of heterogeneous surface film growth mechanisms in lithium-ion batteries. Journal of The Electrochemical Society, 2017, vol. 164, no 11, p. E3335-E3344.

(8) Peled, E.; Menkin, S. SEI: past, present and future. Journal of The Electrochemical Society, 2017, vol. 164, no 7, p. A1703-A1719.

Funded by the European Union